Improving the Image Acquisition Rate of an Atomic Force Microscope Through Sub-sampling and Reconstruction

Roger A. Braker, Yufan Luo, Lucy Y. Pao and Sean B. Andersson

Abstract—Undersampling-based approaches in Atomic Force Microscopy (AFM) aim to reduce the time to acquire an image by reducing the number of measurements needed while still maintaining image quality. In this paper, we describe a hardware implementation and demonstration of one such approach based on the use of collections of short scans known as μ–paths. Using a commercial AFM, we acquire data on a grating sample. Reconstructions are made from these data using a new variant of basis pursuit, Basis Pursuit with Vertical Variation (BPVV), that is designed to reduce artifacts arising from the sampling pattern. The quality of the resulting images is compared to images from standard raster scans of the same regions at comparable imaging rates using both the peak signal-to-noise ratio and the structured similarity index metric and a new metric we call the relative damage index. These experiments demonstrate that at slow scan rates, the μ–path scheme produces similar image quality with significantly less sampling (and thus less tip-sample interaction) and that at high rates, the undersampling scheme produces higher quality images than raster scanning.

I. INTRODUCTION

The Atomic Force Microscope (AFM) is a powerful instrument capable of imaging sample surface topography, material characteristics, and other surface properties, with nanometer scale precision. AFMs acquire information about the sample by monitoring the deflection of the cantilever caused by the tip-sample interaction force. In general, feedback control is used to hold the deflection signal constant and information about the property of interest is inferred from the applied control or the measured dynamics of the cantilever [1]. Because of its versatility, spatial resolution, and ability to image in vacuum, air, and liquid, AFM is widely used in a variety of disciplines, including physics, biology, and materials science [2]–[6].

In addition to imaging static samples, AFM is used to study dynamics in systems with nanometer-scale features [3], [7]–[9]. The image acquisition time of conventional AFMs, however, is typically on the order of seconds to minutes, severely limiting the time-scales that can be explored. Driven by the need for faster imaging, there continue to be many active research efforts to overcome this challenge. Since an

AFM is fundamentally a mechanical microscope, many of the approaches to high-speed AFM (HS-AFM) have focused on modifications to the physical components. These have included the use of small, fast cantilevers [10]–[12], the development of faster actuators [13]–[15], as well as the application of advanced controllers [16]–[19]. By combining different techniques, there are current generation, high-end instruments that can image at rates on the order of 1-10 frames/sec [9]. However, the fastest rates are achieved only over small scan ranges and there remain many systems of interest whose dynamics are faster even than these instruments can achieve. In addition, there is a large installed base of much slower AFMs that can benefit from alternative approaches to improving imaging rate.

A complimentary class of HS-AFM approaches considers modifications to the sampling scheme rather than the system mechanics. Alternative scan trajectories like spirals, cycloids, and Lissajous figures, have been used in place of the standard raster scan. These trajectories are easier for the actuators to follow, allowing the tip to be moved more quickly and leading to faster image acquisition on an otherwise unmodified instrument [20]–[24]. Such approaches are ultimately limited by the vertical bandwidth of the instrument for regulating the deflection signal [25]. Related to these are local scanning methods that use the measurements in real-time to steer the tip to focus the scan on features of interest, reducing imaging time by reducing the amount of sampling needed [26]–[29]. While these have been shown to yield an order of magnitude or better improvement in imaging rate, they are limited in the class of samples that can be imaged.

An alternative group of non-raster scanning schemes, introduced in [30], [31], is based on the idea of undersampling. As with local scanning, data acquisition time is reduced by reducing the amount of measurements acquired. Unlike local scanning methods, this approach still presents the full image. Taking advantage of the redundancy in many natural signals of interest, the final surface image can be recovered from the limited number of measured pixels using a variety of different reconstruction methods such as inpainting or schemes based on the theory of compressive sensing (CS) [32], [33]. In addition to the reduced imaging time, undersampling schemes also reduce tip-sample interactions, thereby reducing the likelihood of tip wear or sample damage.

One simple way to create undersampling schemes is by modifying existing full scan patterns including raster, spiral, and Lissajous scanning. For example, subline sampling is

generated by randomly skipping some of the horizontal lines in raster scanning [32], [34]. For spiral and Lissajous patterns, the scan parameters (frequency and amplitude) can be selected to ensure the trajectory only passes through a desired fraction of the pixels in the final image. The scanning time for these smooth undersampling patterns can be estimated based on the proportion of the pixels in the trajectory. However, results in the literature of CS make clear that *randomness* in the sampling pattern is essential for creating good reconstructions in the general case. The smooth nature of these patterns reduces their randomness and thus leads to less accurate reconstructions than a completely random sampling of the pixels for the same sampling fraction.

In AFM, implementing a truly random pattern requires that the tip be engaged with the surface to collect a measurement, lifted and moved to the new location, and engaged again. Because the re-engagement process is typically slow, this can lead to excessively long image acquisition times and negate the gains from undersampling [31]. In [35], we introduced a discrete undersampling scheme, called a μ-path pattern, which consists of short randomly placed, horizontal scans (see Fig. 1 for one such pattern). It is designed to balance the randomness needed (to ensure good reconstruction) with continuous scanning (to reduce the number of tip engagements).

Our previous work on the μ-path pattern, using theoretical calculations, simulations, and a preliminary implementation, demonstrates that the approach can achieve scanning time reduction while maintaining faithful image reconstruction [35]–[37]. The main contributions of this paper relative to that past work are:

- We introduce a new reconstruction algorithm which is designed to minimize the artifacts arising from the structure of the μ-path scanning pattern. This algorithm is described and compared to existing reconstruction methods through simulations in Sec. II.
- In our prior experimental prototype [37], we used very basic integral controllers for all three axes for both raster and μ-path scans. Here, we design compensators for each axis using standard loop-shaping techniques (Sec. IV-C), which result in a substantial increase in closed-loop bandwidth (e.g., 50 Hz to 450 Hz for the Z-axis). We show in Sec. IV-D that one of the limitations of μ-path scanning is the discontinuous X-axis reference (e.g., in moving between μ-paths) which excites the cross-coupling modes between the X and Z axes, an affect which neither our prior experimental work nor the numerous simulation studies have accounted for. We mitigate the cross coupling with a feed-forward design.
- We experimentally compare (Sec. VI) μ-path scanning to not only full density raster scans but also to coarse raster scans which are interpolated to a full image. This is in contrast to typical sub-line sampling which takes scan lines at random. The clear advantage to a coarse raster scan is that it requires no modification to the instrument, only to the post-processing.
- The bulk of this work is based on experiment, not simulation, in contrast to prior work by ourselves [38], [39] and others [40]–[42]. Our main focus here is on
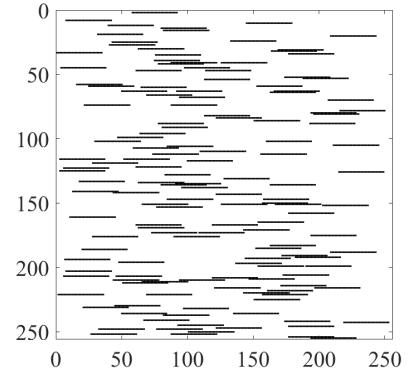

Fig. 1: An example of the horizontal μ-path sampling pattern for a 256×256 pixel image with 35 pixels in each short scan and a total of 20% pixels scanned.

delineating the practical issues which must be addressed to effectively realize μ-path scanning, which has only seen limited attention in the past.

II. RECONSTRUCTION METHODS

Compressive sensing (CS) is a signal processing technique which aims at signal reconstruction from a relatively small (sub-Nyquist limit) number of measurements [43]. It takes advantage of the approximate sparsity of real-world signals, that is, that many coefficients of such signals are close to zero when represented in an appropriate basis. CS methods seek the true image signal $x \in \mathbb{R}^n$ from the observation equation,

$$y = Rx = RU\eta, \tag{1}$$

where $y \in \mathbb{R}^m$ is the observation vector, R is an $m \times n$ matrix defining the measurements, U is an $n \times n$ sparsity basis and η is the sparse representation of x in the domain of U. In general, $m \ll n$. In an imaging application, where the underlying signal is a matrix $X \in \mathbb{R}^{h \times s}$, we take $x = \text{vec}(X)$, where the $\text{vec}(\cdot)$ operator stacks the columns of a matrix.

In the AFM application, the probe can only measure a single pixel at a time. Thus the rows of R are a subset of the rows of an n by n identity matrix. Ideally, the sparsity basis and the measurement matrix R will have a low *mutual coherence*, a measure of how each of the rows of R (the measurements) "spreads out" in the domain of U [44]. In the following, we assume that $U^T U = I$, though in the simulation and experimental results, we take U^T as the Discrete Cosine Transform (DCT). The DCT basis generally keeps a good balance between achieving a low mutual coherence between U and the μ-path sensing matrices R and providing a high sparsity for typical AFM sample images.

Basis pursuit with denoising (BPDN) is one common realization of the CS-based reconstruction problem, and is given by the optimization

$$\min_x \left\| U^T x \right\|_1 \quad \text{s.t.} \quad x \in Q_p = \{x : \ \|Rx - y\|_2 < \sigma\} \tag{2}$$

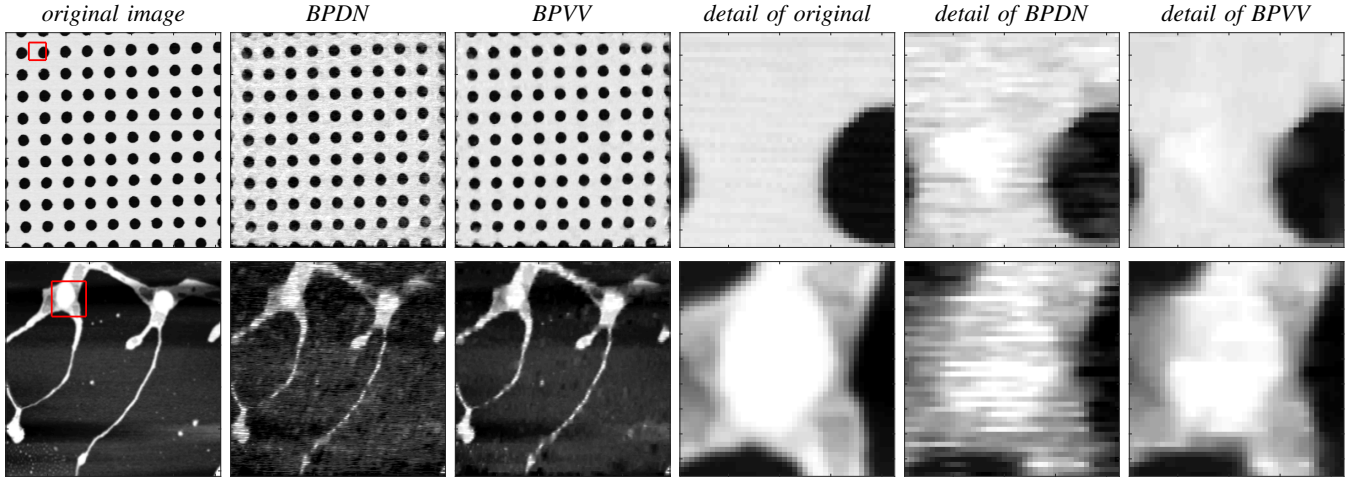| original image	BPDN	BPVV	detail of original	detail of BPDN	detail of BPVV

Fig. 2: Reconstruction comparison between BPDN and BPVV. (first column) Original raster-scanned image. (second column) BPDN reconstruction from random, 40 pixel long μ-paths with 25% sampling. (third column) BPVV reconstruction from the same sub-sampled data. (remaining columns) Corresponding details from the red boxes indicated in the raster image. The results show that BPVV reduces the artifacts arising from the horizontal scans of the μ-path pattern that appear in BPDN reconstructions.

where σ represents uncertainty in the measurements. BPDN essentially searches for the sparsest signal from all the candidates that match the measurements.

Although BPDN is effective in the general setting, using it for reconstruction from horizontal μ-path samples often yields artifacts in the vertical direction (that is, the direction orthogonal to the μ-path scans) leading to strong discontinuities in the image. These artifacts grow more prominent as the length of the μ-paths is increased [35], because these longer paths lead to increased mutual coherence between the measurement matrix R and the sparsity basis U. However, longer μ-paths means fewer μ-paths and thus shorter scan times.

To mitigate these affects, we propose a new variant of BPDN that we term basis pursuit with vertical variation (BPVV). BPVV adds a vertical total variation penalty in the spatial domain to the optimization objective. That is, (2) is modified to

$$\min_{x \in Q_p} f(x) = \min_{x \in Q_p} \left\| U^T x \right\|_1 + \alpha \left\| D_v x \right\|_1 + \beta \left\| D_h x \right\|_1 \quad (3)$$

$$= \min_{x \in Q_p} \left\| W^T x \right\|_1 \quad (4)$$

where

$$W = \begin{bmatrix} U^T & \alpha D_h & \beta D_v \end{bmatrix}$$

with $D_v x = \text{vec}(\nabla_v X)$ (resp., $D_v x = \text{vec}(\nabla_v X)$) representing a discrete gradient of a matrix in the vertical (resp., horizontal) direction (see, e.g., [45, Sec. 6.1,]). Thus, in (3), $\left\| D_v x \right\|_1$ (resp., $\left\| D_h x \right\|_1$) is the total variation (TV) of the signal in the vertical (resp., horizontal) direction. The parameters α and β are weighting parameters. The description of BPVV in (4) can be interpreted as changing our assumption of sparsity in the DCT basis to assuming sparsity in an overcomplete dictionary [46]. When written as (4), the problem is in a form that may be solved with NESTA [45].

A simulation comparison between BPDN and BPVV is shown in Fig. 2. The first column shows two raster scans: the

top is 512 by 512 pixel image of a CS20NG grating acquired with an Agilent 5400 AFM and the bottom is a 256 by 256 pixel image of DNA acquired with an Agilent 5500 AFM. For the CS20NG grating, we sampled 15% of the pixels with 50 pixel μ-paths. We sampled 25% of the DNA image with 25 pixel long μ-paths. The second columns shows the full frame reconstructions using BPDN and the third columns shows the result using BPVV. The fourth column zooms in on the region indicated by the red box in column one. Similarly, the fifth and six columns show the detail of the reconstructions. The reconstruction results show the artifacts apparent in the BPDN reconstruction are largely mitigated using BPVV. Thus, in the remainder of the paper, we focus exclusively on BPVV. As for reconstruction time, it took about 1.5 seconds to reconstruct the DNA image and about 7 seconds for the CS20NG.
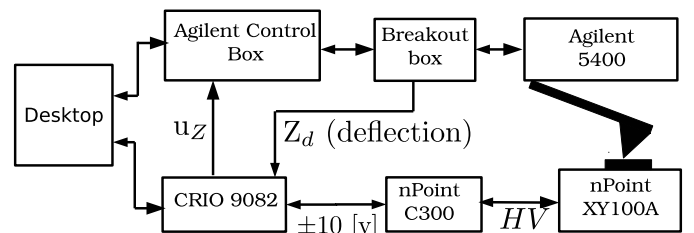
III. EXPERIMENTAL SETUP

Fig. 3: Schematic diagram of the experimental AFM setup.

Our experimental setup, illustrated in Fig. 3, consists of an Agilent 5400 AFM retrofitted with an nPoint NPXY100A piezoelectric stage, a cRIO-9082 embedded controller (National Instruments), and a standard desktop computer.

Through a breakout box, the Agilent 5400 provides access to the Z-axis deflection signal. When the Agilent software is set to open-loop mode, a ± 10 volt input on the standard control

box allows control of the Z-axis of the N9524a piezo scanner, which has a total range of 7 μm. Initial (course) engagement of the tip to the sample is performed using the PicoView software before control is handed over to the custom controllers.

All control logic is programmed using LabVIEW 2019 and compiled to a Xilinx Spartan-6 LX150 Field Programmable Gate Array (FPGA) inside the cRIO-9082. The cRIO includes a 16-Bit, 100 kHz NI-9215 analog-to-digital input module and a 16-Bit, 100 kHz NI-9263 digital-to-analog output module. All control loops are implemented using a 25 kHz sampling rate.

IV. Implementation

Implementing the μ-path scheme involves operating the AFM in several distinct stages. In the XY-direction, the system transitions from tracking a step command in the transition to a new measurement location to tracking a short ramp during the actual μ-path scan. In the Z-direction, the system must transition between tip descent, surface scanning, and tip retraction. Two cycles of this sequential process are illustrated by the time series in Fig. 4. The following subsections describe in more detail several features of the CS scanning process.

Transition between, and operation in, these different stages is implemented as a simple state machine, summarized in Table I. The main job of the state machine is to adjust the reference signals to accomplish each task. In the following, r_X and r_Y and r_Z refer to the references for the X and Y axes while $r_{Z,s}$ and $r_{z,\text{up}}$ refer to the Z-axis setpoints during scanning and retraction, respectively.

TABLE I: Summary of the tasks for μ-path scanning.

state	r_X, r_Y	r_Z	next-state
(1) XY-move	setpoint	$r_Z = r_{z,\text{up}}$	(2)
(2) tip-engage	setpoint	$r_Z = r_{z,s}$	(3)
(3) pre-scan	ramp	$r_Z = r_{z,s}$	(4)
(4) μ-path scan	ramp	$r_Z = r_{z,s}$	(5)
(5) tip up	setpoint	$r_Z = r_{z,\text{up}}$	(1)

A. Cantilever does not need to fully disengage.

In our initial implementation [37], we insisted that the during tip-retraction (state-5), the cantilever tip should fully break contact with the surface. Here, we impose no such requirement. Rather, we change the Z-setpoint during tip-retraction to only pull away far enough that the deflection signal stays low (i.e., below the scanning setpoint), even while we run across the surface. We choose $r_{z,\text{up}}$ so that the interaction between the tip and sample becomes purely adhesive. In general, stable imaging in is not possible at $r_{z,\text{up}}$ and complete dis-engagement occasionally occurs. This can be seen in bottom pane of Fig. 4 during the second XY-move (black portion) where the tip detaches partway through the move. When dis-engagement does occur, the Z-axis control loop implements an anti-windup scheme to prevent the control from saturating.

Only moving the tip into the adhesive region during the XY move saves considerable time compared to completely detaching the tip between each μ-path. By eliminating the normal
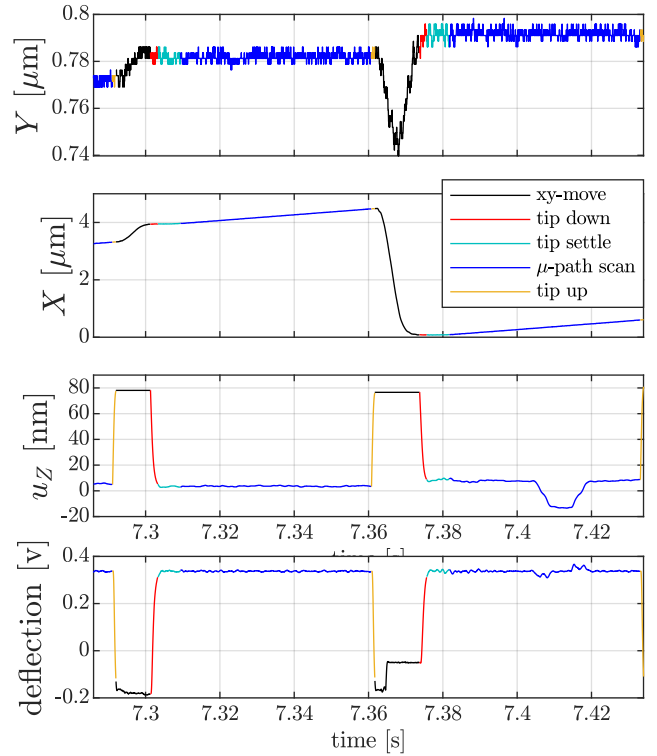

Fig. 4: Several CS cycles. Each state is indicated by color.

force into the sample, we are able to take dozens of images with a single probe without a noticeable degradation in image quality. However, completely characterizing the damage done to the tip and sample with this scheme compared complete detachment (which can also damage the probe [47]), remains an outstanding goal.

B. The pre-scan

After the tip-descent, we begin scanning in a "pre-scan" phase (state (3)), which is the turquoise portion of the trajectories in Fig. 4. There are two reasons for this. First, we have observed that there is less noise in the deflection signal while the XY-stage is in motion compared to sitting still. More importantly, it lets us bring the X-axis to its scanning velocity at the same time the transients from the Z-axis die out. Without this, we must extend the μ-path by a distance equal to the steady-state error following a ramp. For an arbitrary scan speed, this means the μ-path scan would need an extra

$$N = \left\lceil \lim_{z \to 1} \frac{1 - H_x}{z - 1} \right\rceil \qquad (5)$$

time steps, where H_x is closed-loop transfer function for the x-axis. For our system $N = 111$. By initiating the scan while the Z-axis settles, we eliminate much of this overhead.

C. Control

The control structure for each axis, shown in the block diagram in Fig. 5, is similar and essentially consists of a set of filters in series with a PI controller. The open-loop frequency response for the X and Y axes is shown as the black curves

$$
\begin{bmatrix} r_X \\ r_Y \\ r_Z \end{bmatrix}
\rightarrow
\begin{bmatrix} F_X & & 0 \\ & F_Y & \\ 0 & & 1 \end{bmatrix}
\rightarrow +\ \Sigma\ -
\rightarrow
\begin{bmatrix} \frac{zk_X}{z-1} & & 0 \\ & \frac{zk_Y}{z-1} & \\ 0 & & \frac{zk_Z}{z-1} \end{bmatrix}
\rightarrow
\begin{bmatrix} D_X & & 0 \\ & D_Y & \\ 0 & & D_Z \end{bmatrix}
\rightarrow
\begin{bmatrix} \mathcal{H}_X^{-1}[\cdot] \\ 1 \\ 1 \end{bmatrix}
\rightarrow
\text{Plant}
$$

Plant:
$$
\begin{bmatrix}
G_{X,u_X} & G_{X,u_Y} & G_{X,u_Z} \\
G_{Y,u_X} & G_{Y,u_Y} & G_{Y,u_Z} \\
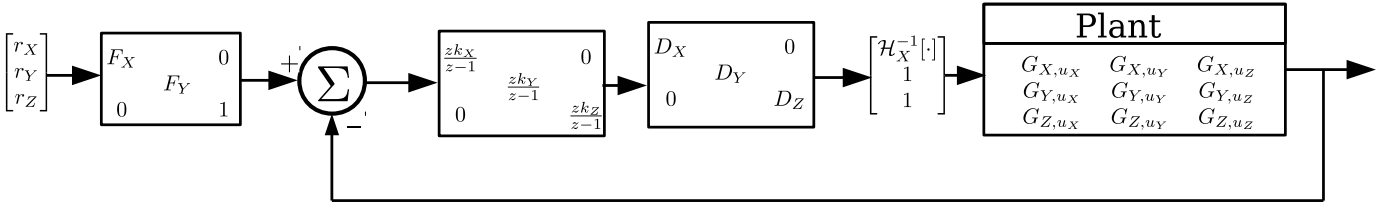G_{Z,u_X} & G_{Z,u_Y} & G_{Z,u_Z}
\end{bmatrix}
$$

Fig. 5: Block diagram of the Z-axis control loop. The anti-windup is active for decision index $i \in \{0,1,5\}$, which correspond to states such that $r_Z = r_{z,\mathrm{up}}$.

in Fig. 6a and for the Z-axis in Fig. 6c. The first resonance of each axis is the bending mode, which appears at 215 Hz for the Z axis and about 350 Hz for the X and Y axes.

The filter portion of the Z-axis controller D_Z is second-order and simply inverts the complex-conjugate pole-zero pair at 215 Hz. This allows the gain of the PI controller to be increased substantially. The closed-loop achieves a bandwidth of about 450 Hz, as shown by the red curve in Fig. 6c. Without this inversion, the bandwidth is limited to about 50 Hz.

We take a similar approach for the X and Y axes. The filters D_x and D_y invert the bending modes at 350 Hz and add notch filters at the main resonant peaks near 650 Hz. The resulting closed-loop transfer functions are shown as the red curves in Fig. 6a.

In general, the X-axis positioning requirements are more stringent for both CS and raster scanning. Due to the step inputs the X-axis must track, we have found that compensating hysteresis and creep to be particular helpful during μ-path scanning. Thus, the X-axis compensator also includes an inverse creep and hysteresis model. The hysteresis model is a modified Prandtl-Ishlinki type model and is based on the work of [48], while the drift compensation models the piezo creep as a simple second order transfer function with real poles and zeros. In Fig. 5, the hysteresis inversion is indicated by $\mathcal{H}^{-1}[\cdot]$. We have found that the inclusion of these extra compensators limits the overshoot of the X-axis during larger moves between different μ-paths (e.g., without them, the X-axis trajectory in Fig. 6b would show noticeable overshoot). More details on fitting the creep and hysteresis models can be found in our other work [49].

D. Feedforward Control

Unfortunately, as the bottom row of plots in Fig. 6a makes clear, there is a strong cross-coupling from the horizontal plane to the Z axis (the coupling from u_Z to the X and Y axes is very weak, and so is not shown). Our SISO control scheme does little to attenuate the resonances of G_{Z,u_X} and G_{Z,u_Y}. In particular, there are modes in both these transfer functions at 215 and 505 Hz that do not appear in a SISO model of G_{X,u_X} or G_{Y,u_Y}.

For raster scans, the frequency content of the X-axis reference (which is a triangle wave) decays like $1/n^2$ with a gain proportional to the raster frequency. In contrast, the X-axis reference for a μ-path scan is composed of a sequence of steps and ramps. The inclusion of the (discontinuous) steps means we should expect the μ-path X reference to decay like $1/n$. Thus, while the cross-coupling can induce Z-axis vibrations

for faster raster scans, it is especially problematic for μ-path scanning. This is illustrated in the left column of Fig. 6b, which shows a CS cycle during which the X-axis makes a 5 micron move, which induces excessively large vibrations in the vertical control.

In principle, one could mitigate these issues with a full MIMO control design. In this work, we opt for a much simpler feedforward scheme. For CS scanning, we insert feed-forward filters (F_X and F_Y in Fig. 5) with three notches: one at 215 Hz, one at 350 Hz and one at 505 Hz. Both filters are shown in Fig. 6a as the dashed-pink curves and the resulting overall FRF is shown as the dotted-blue curves, which show a dramatic reduction in the cross coupling. A similar affect could be achieve by using a simple low-pass filter. However, to achieve the same 40 dB of attenuation of the mode at 215 Hz, would require, e.g., that a two-pole low-pass filter have its cut-off frequency at about 20 Hz. Thus, while our feedforward scheme slows the X-axis down, we achieve better bandwidth than we would with a simple low-pass filter.

For raster scanning, we set $F_X = F_Y = 1$ and instead take advantage of the periodicity of the X-axis reference, which is a triangle wave. We modify the triangle wave to a truncated Fourier series, where each Fourier coefficient is scaled by the inverse of the closed-loop FRF at the corresponding frequency. See, e.g., [50] for more details on this strategy. We truncate this series such that the highest frequency is smaller than 200 Hz, which means that we should never excite the problematic G_{Z,u_X} modes. This scheme implies that the effective bandwidth of the X-axis controller is higher while raster scanning than while CS-scanning. On the other hand, it also implies that the for faster scan rates, fewer Fourier coefficients are used, and so the approximation to a triangle wave is worse.

V. METRICS

In section VI we use three metrics to asses our results. The first two seek to quantify image quality of two images. Define a master image as X and a reconstruction or corrupted version as Y, with each having $s \times h = m$ pixels. Let $x = \mathrm{vec}(X)$ and $y = \mathrm{vec}(Y)$. Let L be the dynamic range of the master image x. Then the peak signal to noise ratio (PSNR) is given by

$$
\mathrm{PSNR}(x,y) = 10\log_{10}\frac{L^2}{\sqrt{\frac{1}{p^2}\sum_{i=1}^{m}(x_i - y_i)^2}}.
$$

The goal of the SSIM is to compare two image's structure, luminescence, and contrast and is built up from the means
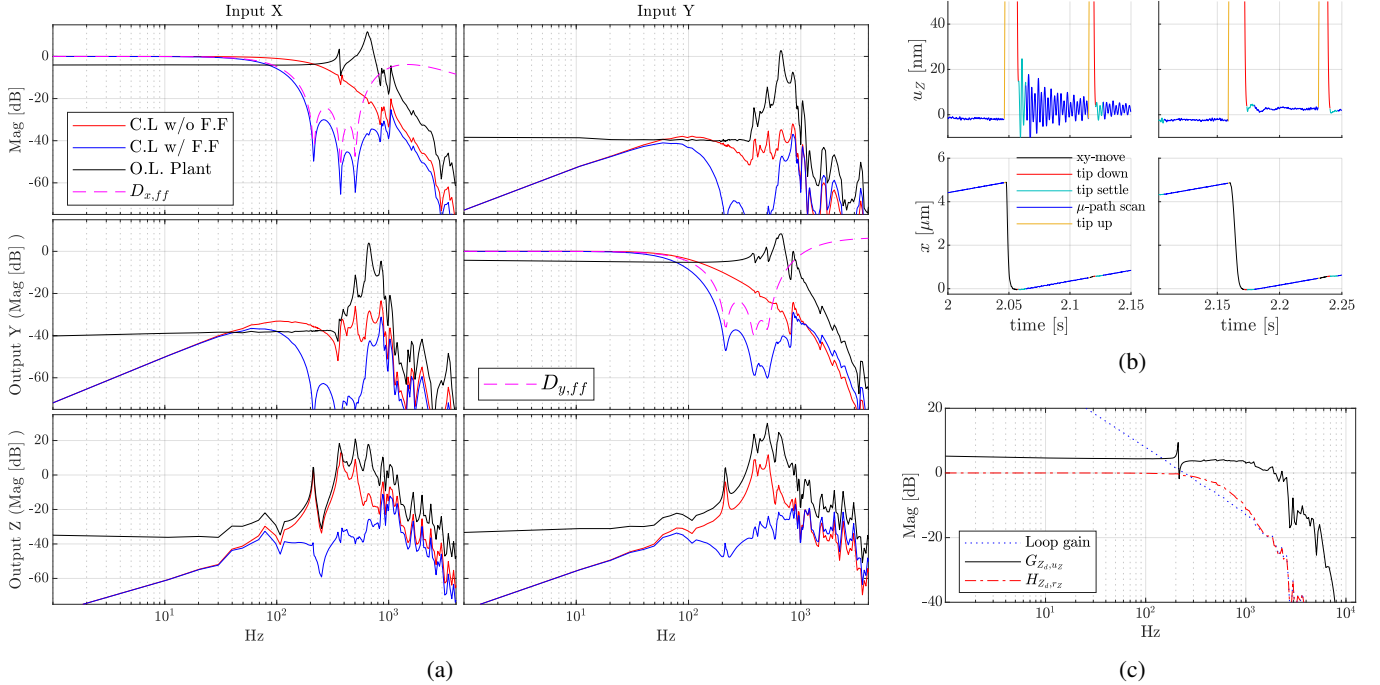
Fig. 6: (a) MIMO closed and open-loop FRFs, showing the dramatic affect on G_{Z,u_X} and G_{Z,u_Y} when the feedforward compensators are used for the X and Y axes. (b) The vertical control u_Z (top) after a large move in the X-direction (bottom) without (left column) and with (right column) the feedforward compensation. (c) Frequency response of the Z-axis in open-loop (black) and closed-loop (red).

(μ_x and μ_y), standard deviations (σ_x and σ_y), and covariance (σ_{xy}) of the image vectors x and y. The variation of the SSIM used in this paper is defined as

$$\text{SSIM}(x,y) = \frac{(2\mu_x\mu_y + C_1)(2\sigma_{xy} + C_2)}{(\mu_x^2 + \mu_y^2 + C_1)(\sigma_x^2 + \sigma_y^2 + C_2)}$$

where the constants C_1 and C_2 are regularizing constants to prevent singularity if, e.g., $\mu_x = \mu_y = 0$. We use the default values suggested in [51] of $C_1 = (0.01L)^2$ and $C_2 = (0.03L)^2$, where again, L is the dynamic range. In general two images which are identical will yield an infinite PSNR and an SSIM of 1.

A. Limitations of SSIM and PSNR

The SSIM and PSNR have become reasonably popular in studies comparing simulated AFM image reconstructions [38], [40], [42]. However, it remains somewhat of an open question how to best compare experimental AFM images. While we use the SSIM and PSNR in Sec. VI, we believe those numbers should be interpreted with some caution. In our experimental setup, actuation in the XY-plane happens via the nPoint piezo stage and the XY-direction of the original piezo scanner is uncontrolled. This leads to substantial drift between images. To illustrate this, we took a sequence of 6 raster scans of a sample grating, each at a 1 Hz scan rate over a 5 micron by 5 micron area. The left image of Fig. 7 shows the error between the first and sixth image. The PSNR and SSIM between the first and second images are 15.08 and 0.51; between the first and sixth are 8.49 and 0.26, respectively, even though on their own each image appears to have good quality.
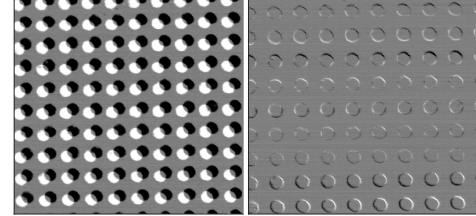

Fig. 7: Errors between the first and sixth raster scans in a sequence of six 1.0 Hz raster scans. (left) Errors without alignment (right) The same data but aligned via cross correlation.

To mitigate this affect, we use an image alignment technique based on the 2D cross-correlation between each image. Essentially, this takes a sub-slice of the master (first) image (here, a 25 pixel inset on each edge), and finds the offset in the other image that produces the smallest error. The result of this procedure are shown in the right image of Fig. 7. Although the situation is improved compared to the un-aligned images, there is still noticeable stretching (the upper and lower portions appear considerably worse than the middle). Notably however, with the alignment technique, the SSIM is 0.72 for both the second and sixth image images and the PSNR is increases to 23.40 and 22.68 respectively.

B. A new metric

Th PSNR and SSIM metrics only assess the similarity of two images. However, in AFM imaging, pure image quality is not the only concern, particularly for delicate samples. What

is needed is a figure of merit for how much damage was done to specimen during the imaging process. While damage to the specimen is not really a concern while imaging a hard calibration grating, it plays a prominent role for biological samples [52], though damage to the probe itself is still a concern. In general, the faster the scan rate, the more difficulty the Z-axis control will have following the sample surface, which results in a larger Z_d over more time. The actual damage done by a given Z_d will depend on the spring constant of the cantilever and the softness of the specimen. Nonetheless, we propose a metric, which we call the Relative Damage Index (RDI) which computes the power in the deflection signal for a given scan. That is,

$$\text{RDI} = \frac{1}{T_s} \sum_{k=0}^{N} \frac{1}{k} \left(Z_{d,k} - r_{Z,s} \right)^2 \tag{6}$$

$$\tag{7}$$

The idea behind the RDI is that increased scan rates lead to larger deflection signals (and thereby increased force into the specimen) at each surface feature, which the RDI accumulates.

VI. EXPERIMENTAL RESULTS

We compared μ-path scanning to two scenarios. First, we compare it to full resolution raster scans at several scan rates in Sec. VI-A. Second, we compare to course raster scans in Sec. VI-B.

A. Comparison to full raster

We took scans of a Ted Pella CS-20NG sample grating over an area with holes on a 500 nm pitch. The holes are 20 nm deep. We scanned 5 micron by 5 micron images using standard raster scans with 512 lines. For the raster scans, we took scans at 1.0 Hz, 2.5 Hz, 5.0 Hz, 8.0 Hz and 10 Hz. We also took μ-path scans with densities at 12.5%, and 25% and reconstructed 512 by 512 pixel images. The CS scans were taken with scan velocities equivalent to raster scan rates of 1.0 Hz, 2.0 Hz, 5.0 Hz and 8.0 Hz. For all CS scans, the μ-paths are 500 nm long, which translates to 51 pixels.

The free value of the deflections signal was approximately -0.6 volts and we set the scanning reference to $r_{z,s} = -0.3$ volts (for both raster and CS) and the withdraw reference to $r_{z,\text{up}} = -0.8$ volts. We set the XY-settle boundary to ± 0.02 microns and required 20 samples within this boundary before moving to the Z-engage state. The pre-scan length was 150 time steps. The cantilever was a Budget Sensors ContAI-G, with a nominal length of 450 microns and spring constant of $k = 0.2$ N/m.

The CS scans were reconstructed with BPVV. We set $\alpha_v = 0.1$ and $\alpha_h = 0.75$. For the raster scans, we discard data from the re-trace and divided the remaining data for each scan line into 512 bins based on the X sensor measurements. We then average the data in each bin to obtain the value of one pixel. To remove the affects of piezo creep and sample tilt, we then de-trend each individual line. De-trending each line causes the flat portion between the holes in the horizontal

TABLE II: Breakdown of state times for the CS scans shown in Fig. 8. All times are in seconds.

description	move	engage	pre-scan	scan	tip-up	total
1.0 Hz, 12.5 %	6.16	1.13	3.82	32.25	0.24	43.60
5.0 Hz, 12.5 %	6.09	1.01	3.82	6.73	0.08	17.73
8.0 Hz, 12.5 %	6.14	1.02	3.82	4.35	0.08	15.40
1.0 Hz, 25.0 %	11.84	2.40	7.62	64.41	0.15	86.42
5.0 Hz, 25.0 %	11.54	2.19	7.62	13.44	0.53	35.32
8.0 Hz, 25.0 %	11.73	2.06	7.62	8.68	0.15	30.25

direction to appear at a different height than the flat portion between holes in the vertical direction. To remove this effect, we select a column of pixels on the left and right side of each image that does not cross any holes (i.e., a vertical line through the flat area), register each scan line to a common height along these columns. This step eases comparison with the CS scans and was inspired by a feature in the AFM image processing toolbox SPIW [53]. The resulting images are shown in Fig. 8. The color maps represent a range of ± 20 nm. The rows of pixels indicated by the red lines are shown as cross sections Fig. 9.

For each raster scan and each CS scan, we computed the SSIM and PSNR using the 1 Hz raster scan as the master and also computed the RDI metric. These are plotted against total acquisition time in Fig. 10a and 10b. Unfortunately, the SSIM and PSNR metrics are not particularly illuminating. There are several inconsistencies. For example, it makes no sense the 1 Hz CS scan at 25% has a *worse* PSNR and SSIM than 5 Hz version; nor does it make sense that the 8 Hz full raster scan has a worse SSIM and PSNR than the 10 Hz full raster scan.

Things are clearer if we plot the RDI for each scan against total acquisition time, which is shown in Fig. 10c and this is where CS seems to shine. As one would expect, as imaging time decreases, the RDI for each scan type increases. From Fig. 10c, we see that for a fixed RDI, CS has a faster imaging acquisition rate. The amount of improvement is best if we need a very low RDI: for example, if we want to hold the RDI below 2, then we have to take the 1 Hz raster scan (512 seconds) while we can achieve the same RDI via CS in about 42 seconds with the 12.5% sampling, which is a speed improvement of over 10. The higher of an RDI we are willing to tolerate, the advantage of CS over raster narrows. For example, the 8 Hz raster scan and 8 Hz, 12.5% CS scan have comparable RDIs, but now CS is only about 5 times faster. This is a result of the constant overhead imposed by the engage/disengage and XY-move states in CS which remains constant for different scan rates.

B. Comparison to Sub-line Sampling

Many of sub-line sampling papers assume that the lines to sample are selected randomly [38], [40]. An even simpler alternative to μ-path sampling is to simply take a standard raster scan with fewer lines. This is the technique we consider in this subsection, by scanning images with 128 and 64 lines. For each of these scenarios, we first divide the data for each line into 512 bins. This gives an image that is 128 (resp., 64) pixels by 512 pixels. We then linearly interpolate along each column to produce a 512 by 512 pixel image. Again, we take
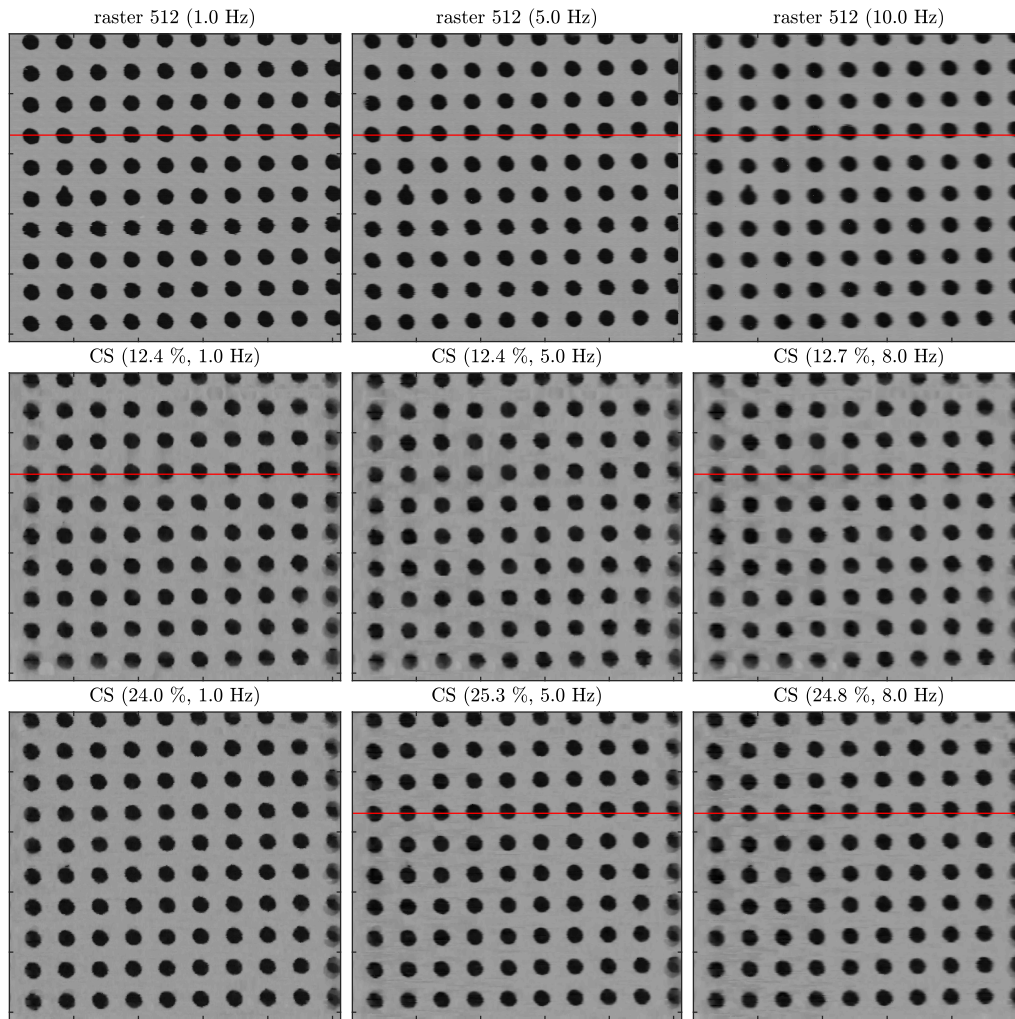
Fig. 8: Raster and compressed sensing images of a 5 micron square area of the CS-20NG grating. All images are 512×512 pixels: the raster images marked as 64 and 128 lines have been interpolated. The rows of pixels indicated by the red line are shown in Fig. 9.
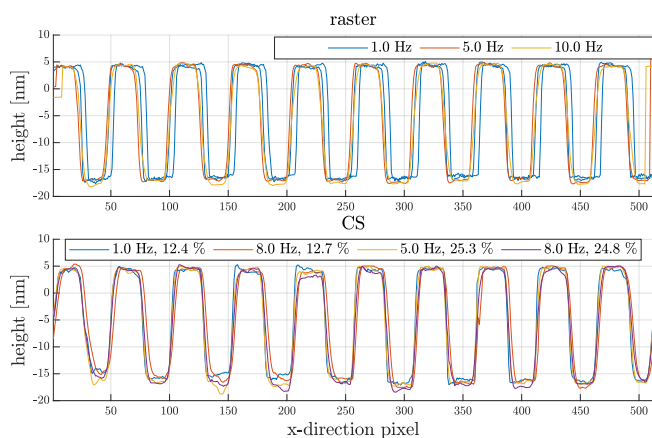

Fig. 9: Rows of pixels, as indicated by the red lines in Fig. 8. For clarity, not all images are included.

these courser raster scans at 1.0, 2.5, 5.0, 8.0 and 10.0 Hz. The resulting images are shown in Fig. 11.

Both visually and from the metrics show in From both From the metrics in Figs.Figs. 10a and 10b, the 64 line scan performs the worst of the all the sub-sampling methods and is slower than 12.5% CS for slow scan rates. However, the 128 line scans appear to have as good or better image quality than either CS scans.

Note the defect on the hole located in the second column, sixth row from the top (of the grating holes). The CS-scans do a poor job detecting this, while both course raster scans do so. However, the other artifacts in 64 line scan obscure the defect.

Fig. 12 compares the amount of speed improvement of the different sub-sampling scheme over a full raster scans with 512 lines as a function of scan rate. As far as pure speed goes, the CS scan at 12.5% is the fastest for a rate of 1 Hz, though the 64 line raster scan is close. At the same time, the image quality of the 1 Hz, 12.5% CS scan is better than the the 1 Hz 64 line raster scan. However, this advantage quickly evaporates for faster scan rates. Indeed, for rates beyond about 5 Hz, the raster scan with 128 lines is not only faster than the
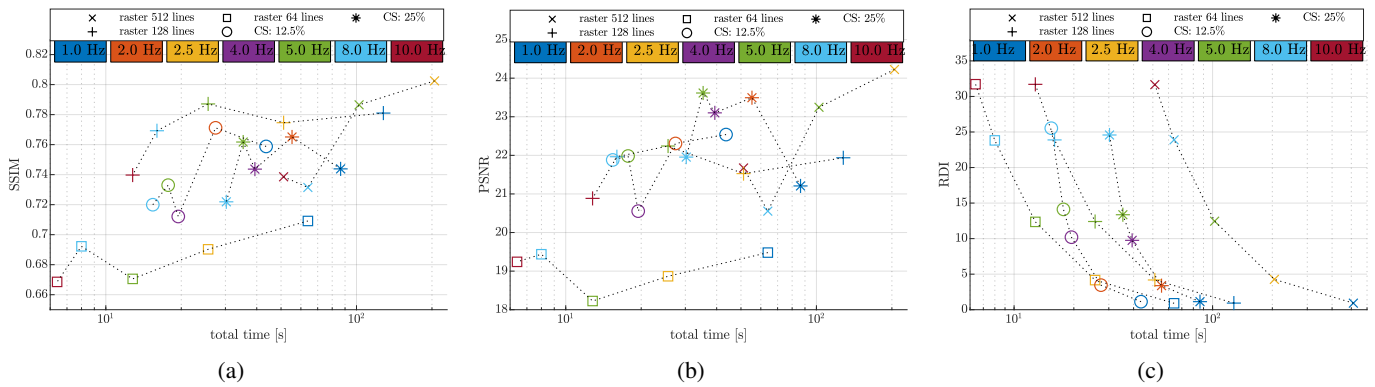
Fig. 10: Metrics for raster scan at 512, 128 and 64 lines and μ-path scans at 12.5% and 25% sampling. The scan rate is indicated by color while the scan style is indicated by marker style. (a) SSIM as a function of total acquisition time. (b) PSNR as a function of total acquisition time. (c) RDI as a function of total acquisition time.

12.5% CS scan, it also has (arguably) better image quality.

VII. CONCLUSIONS

The main conclusion of this paper is that with CS, it seems that we can acquire images faster yet with less specimen damage than is possible while raster scanning a full image. On the other hand, it appears that reconstructing a course raster scan makes more sense for faster scan rates. This is notable, since a course raster scan only requires an additional step in post-processing. It remains to be seen if this conclusion holds for a wide range of instruments.
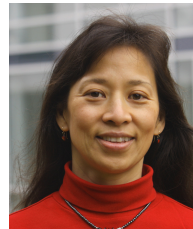
Lucy Y. Pao is probably not so happy that Arnold's almost done.

Roger A. Braker earned the B.A. degree in physics from the University of Oklahoma in 2005 and the M.S. degree in electrical engineering from the University of Colorado in 2017. Since 2014, he has been a graduate student in the Electrical, Computer, and Energy Engineering Department at the University of Colorado Boulder.

Yufan Luo received dual B.S. degrees in automation and in management science from Zhejiang University, Zhejiang, China, in 2011, an M.S. degree in industrial and operations engineering from the University of Michigan, Ann Arbor, MI, USA, in 2012, and a Ph.D. degree in systems engineering from Boston University in 2019. He is currently with Juniper Networks, Sunnyvale, CA.

Sean B. Andersson received the B.S. degree in engineering and applied physics from Cornell University, Ithaca, NY, USA, in 1994, the M.S. degree in mechanical engineering from Stanford University, Stanford, CA, USA, in 1995, and the Ph.D. degree in electrical and computer engineering from the University of Maryland, College Park, MD, USA, in 2003. He has worked at AlliedSignal Aerospace and Aerovironment, Inc. and is currently an Associate Professor of mechanical engineering and of systems engineering with Boston University, Boston, MA, USA. His research interests include systems and control theory with applications in scanning probe microscopy, dynamics in molecular systems, and robotics. He received an NSF CAREER award in 2009, is a senior member of the IEEE, and was an associate editor for the IEEE Transactions on Automatic Control (2014-2018) and for the SIAM Journal on Control and Optimization (2013-2018).
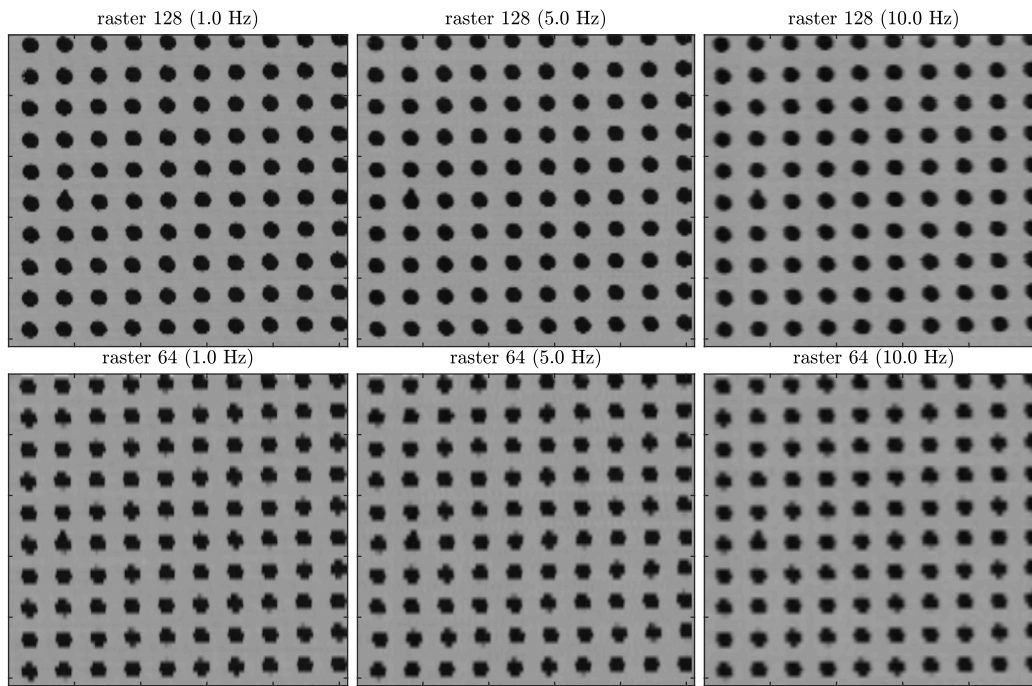
Fig. 11: Raster scans at 128 (top) and 64 (bottom) which have been interpolated along each column to 512 lines.
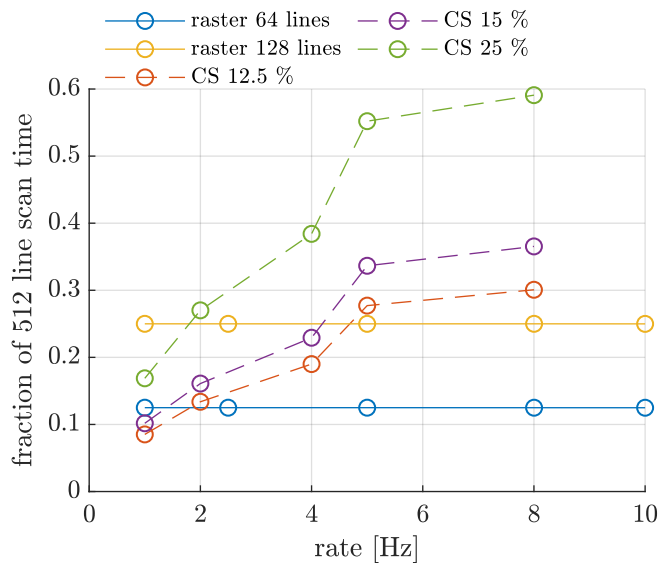

Fig. 12: Fraction of improvement in total scan time over a scan with 512 lines vs scan rate for the three sets of CS scans (at 25%, 15% and 12.5%) and courser raster scans at 128 and 64 lines.

REFERENCES

[1] D. Y. Abramovitch, S. B. Andersson, L. Y. Pao, and G. Schitter, "A tutorial on the mechanisms, dynamics, and control of atomic force microscopes," in *Proc. American Control Conference*, 2007, pp. 3488–3502.

[2] Y. F. Dufrêne, T. Ando, R. Garcia, D. Alsteens, D. Martinez-Martin, A. Engel, C. Gerber, and D. J. Muller, "Imaging modes of atomic force microscopy for application in molecular and cell biology," *Nature Nanotechnology*, vol. 12, no. 4, pp. 295–307, Apr. 2017.

[3] C. Yang, R. Winkler, M. Dukic, J. Zhao, H. Plank, and G. E. Fant-
ner, "Probing the morphology and evolving dynamics of 3D printed nanostructures using high-speed atomic force microscopy," *ACS Applied Materials & Interfaces*, vol. 9, no. 29, pp. 24 456–24 461, July 2017.

[4] O. D. Payton, L. Picco, and T. B. Scott, "High-speed atomic force microscopy for materials science," *International Materials Reviews*, vol. 61, no. 8, pp. 473–494, June 2016.

[5] E. I. Altman, M. Z. Baykara, and U. D. Schwarz, "Noncontact atomic force microscopy: An emerging tool for fundamental catalysis research," *Accounts of Chemical Research*, vol. 48, no. 9, pp. 2640–2648, Aug. 2015.

[6] K. Haase and A. E. Pelling, "Investigating cell mechanics with atomic force microscopy," *Journal of the Royal Society Interface*, vol. 12, no. 104, pp. 20 140 970–20 140 970, Mar. 2015.

[7] M. Shibata, H. Nishimasu, N. Kodera, S. Hirano, T. Ando, T. Uchihashi, and O. Nureki, "Real-space and real-time dynamics of CRISPR-Cas9 visualized by high-speed atomic force microscopy," *Nature Communications*, vol. 8, no. 1, p. 1430, Nov. 2017.

[8] M. Shibata, T. Uchihashi, T. Ando, and R. Yasuda, "Long-tip high-speed atomic force microscopy for nanometer-scale imaging in live cells," *Scientific Reports*, vol. 5, no. 1, p. 8724, Mar. 2015.

[9] T. Ando, T. Uchihashi, and S. Scheuring, "Filming biomolecular processes by high-speed atomic force microscopy," *Chemical Reviews*, vol. 114, no. 6, pp. 3120–3188, Jan. 2014.

[10] M. B. Viani, T. E. Schaeffer, G. T. Paloczi, L. I. Pietrasanta, B. L. Smith, J. B. Thompson, M. Richter, M. Rief, H. E. Gaub, K. W. Plaxco, A. N. Cleland, H. G. Hansma, and P. K. Hansma, "Fast imaging and fast force spectroscopy of single biopolymers with a new atomic force microscope designed for small cantilevers," *Review of Scientific Instruments*, vol. 70, no. 11, pp. 4300–4303, 1999.

[11] C. Braunsmann and T. E. Schäffer, "High-speed atomic force microscopy for large scan sizes using small cantilevers," *Nanotechnology*, vol. 21, no. 22, p. 225705, 2010.

[12] J. D. Adams, B. W. Erickson, J. Grossenbacher, J. Brugger, A. Nievergelt, and G. E. Fantner, "Harnessing the damping properties of materials for high-speed atomic force microscopy," *Nature Nanotechnology*, vol. 11, no. 2, pp. 147–151, Feb. 2016.

[13] M. Maroufi, A. Bazaei, and S. O. R. Moheimani, "A high-bandwidth MEMS nanopositioner for on-chip AFM: Design, characterization, and control," *IEEE Transactions on Control Systems Technology*, vol. 23, no. 2, pp. 504–512, Mar. 2015.

[14] Y. K. Yong, S. O. R. Moheimani, B. J. Kenton, and K. K. Leang, "Invited review article: High-speed flexure-guided nanopositioning: Mechanical

design and control issues," *Review of Scientific Instruments*, vol. 83, no. 12, p. 121101 (22 pages), Dec. 2012.

[15] B. J. Kenton and K. K. Leang, "Design and control of a three-axis serial-kinematic high-bandwidth nanopositioner," *IEEE Transactions on Mechatronics*, vol. 17, no. 2, pp. 356–369, Apr. 2012.

[16] M. S. Rana, H. R. Pota, and I. R. Petersen, "A survey of methods used to control piezoelectric tube scanners in high-speed AFM imaging," *Asian Journal of Control*, vol. 20, no. 4, pp. 1379–1399, July 2018.

[17] Y. K. Yong and S. O. R. Moheimani, "Collocated z-axis control of a high-speed nanopositioner for video-rate atomic force microscopy," *IEEE Transactions on Nanotechnology*, vol. 14, no. 2, pp. 338–345, Mar. 2015.

[18] J. A. Butterworth, L. Y. Pao, and D. Y. Abramovitch, "Adaptive-delay combined feedforward/feedback control for raster tracking with applications to AFMs," in *Proc. American Control Conference*, 2010, pp. 5738–5744.

[19] S. Salapaka, A. Sebastian, J. P. Cleveland, and M. V. Salapaka, "High bandwidth nano-positioner: A robust control approach," *Review of Scientific Instruments*, vol. 73, no. 9, pp. 3232–3241, 2002.

[20] A. Bazaei, Y. K. Yong, and S. O. R. Moheimani, "Combining spiral scanning and internal model control for sequential AFM imaging at video rate," *IEEE/ASME Transactions on Mechatronics*, vol. 22, no. 1, pp. 371–380, Feb. 2017.

[21] J.-W. Wu, Y.-T. Lin, Y.-T. Lo, W.-C. Liu, and L.-C. Fu, "Lissajous hierarchical local scanning to increase the speed of atomic force microscopy," *IEEE Transactions on Nanotechnology*, vol. 14, no. 5, pp. 810–819, Sept. 2015.

[22] M. S. Rana, H. R. Pota, and I. R. Petersen, "Spiral scanning with improved control for faster imaging of AFM," *IEEE Transactions on Nanotechnology*, vol. 13, no. 3, pp. 541–550, May 2014.

[23] T. Tuma, J. Lygeros, V. Kartik, A. Sebastian, and A. Pantazi, "High-speed multiresolution scanning probe microscopy based on Lissajous scan trajectories," *Nanotechnology*, vol. 23, no. 18, p. 185501, Apr. 2012.

[24] Y. K. Yong, S. O. R. Moheimani, and I. R. Petersen, "High-speed cycloid-scan atomic force microscopy," *Nanotechnology*, vol. 21, no. 36, p. 365503, Aug. 2010.

[25] Y. R. Teo, Y. Yong, and A. J. Fleming, "A comparison of scanning methods and the vertical control implications for scanning probe microscopy," *Asian Journal of Control*, vol. 28, no. 2, p. 65, Dec. 2016.

[26] B. Hartman and S. B. Andersson, "Feature tracking for high speed AFM imaging of biopolymers," *International Journal of Molecular Sciences*, vol. 19, no. 4, p. 1044, Mar. 2018.

[27] Y. Wen, J. Song, X. Fan, D. Hussain, H. Zhang, and H. Xie, "Fast specimen boundary tracking and local imaging with scanning probe microscopy," *Scanning*, vol. 2018, no. 4, pp. 1–11, Mar. 2018.

[28] K. Zhang, T. Hatano, T. Tien, G. Herrmann, C. Edwards, S. C. Burgess, and M. Miles, "An adaptive non-raster scanning method in atomic force microscopy for simple sample shapes," *Measurement Science and Technology*, vol. 26, no. 3, p. 035401, Feb. 2015.

[29] P. Huang and S. B. Andersson, "Note: Fast imaging of DNA in atomic force microscopy enabled by a local raster scan algorithm," *Review of Scientific Instruments*, vol. 85, no. 6, p. 066101, June 2014.

[30] B. Song, N. Xi, R. Yang, K. W. C. Lai, and C. Qu, "Video rate atomic force microscopy (AFM) imaging using compressive sensing," in *Proc. IEEE Conference on Nanotechnology*, 2011, pp. 1056–1059.

[31] S. B. Andersson and L. Y. Pao, "Non-raster sampling in atomic force microscopy: A compressed sensing approach," in *Proc. American Control Conference*, 2012, pp. 2485–2490.

[32] A. Chen, A. L. Bertozzi, P. D. Ashby, P. Getreuer, and Y. Lou, "Enhancement and recovery in atomic force microscopy images," in *Excursions in Harmonic Analysis, Volume 2*. Springer, 2013, pp. 311–332.

[33] Y. Luo and S. B. Andersson, "A comparison of reconstruction methods for undersampled atomic force microscopy images," *Nanotechnology*, vol. 26, no. 50, p. 505703, 2015.

[34] G. Han, B. Lin, and Y. Lin, "Reconstruction of atomic force microscopy image using compressed sensing," *Micron*, vol. 105, pp. 1–10, 2018.

[35] B. D. Maxwell and S. B. Andersson, "A compressed sensing measurement matrix for atomic force microscopy," in *Proc. American Control Conference*, 2014, pp. 1631–1636.

[36] Y. Luo and S. B. Andersson, "A fast image reconstruction algorithm for compressed sensing-based atomic force microscopy," in *Proc. American Control Conference*, July 2015, pp. 3503–3508.

[37] R. A. Braker, Y. Luo, L. Y. Pao, and S. B. Andersson, "Hardware demonstration of atomic force microscopy imaging via compressive sensing and μ-path scans," in *Proc. American Control Conf.*, June 2018, pp. 6037–6042.

[38] Y. Luo and S. B. Andersson, "A comparison of reconstruction methods for undersampled atomic force microscopy images," *Nanotechnology*, vol. 26, no. 50, p. 505703, 2015.

[39] B. D. Maxwell and S. B. Andersson, "A compressed sensing measurement matrix for atomic force microscopy," in *Proc. American Control Conf.*, June 2014, pp. 1631–1636.

[40] G. Han and B. Lin, "Optimal sampling and reconstruction of undersampled atomic force microscope images using compressive sensing," *Ultramicroscopy*, vol. 189, pp. 85 – 94, 2018.

[41] T. L. Jensen, T. Arildsen, J. Ostergaard, and T. Larsen, "Reconstruction of undersampled atomic force microscopy images: Interpolation versus basis pursuit," in *Proc. Int. Conf. Signal-Image Technology Internet-Based Systems*, Dec 2013, pp. 130–135.

[42] C. S. Oxvig, T. Arildsen, and T. Larsen, "Structure assisted compressed sensing reconstruction of undersampled AFM images," *Ultramicroscopy*, vol. 172, no. Supplement C, pp. 1–9, 2017.

[43] A. Y. Carmi, "Compressive system identification," in *Compressed Sensing & Sparse Filtering*. Springer, 2014, pp. 281–324.

[44] E. Candès and J. Romberg, "Sparsity and incoherence in compressive sampling," *Inverse problems*, vol. 23, no. 3, p. 969, 2007.

[45] S. Becker, J. Bobin, and E. Candès, "Nesta: A fast and accurate first-order method for sparse recovery," *SIAM Journal on Imaging Sciences*, vol. 4, no. 1, pp. 1–39, 2011.

[46] E. J. Candès, Y. C. Eldar, D. Needell, and P. Randall, "Compressed sensing with coherent and redundant dictionaries," *Applied and Computational Harmonic Analysis*, vol. 31, no. 1, pp. 59 – 73, 2011.

[47] E. Meyer, "Atomic force microscopy," *Progress in Surface Science*, vol. 41, no. 1, pp. 3–49, 1992.

[48] K. Kuhnen, "Modeling, identification and compensation of complex hysteretic nonlinearities: A modified Prandtl-Ishlinskii approach," *European J. Control*, vol. 9, no. 4, pp. 407–418, 2003.

[49] R. A. Braker and L. Y. Pao, "A comparison of tracking step inputs with a piezo stage using mpc and saturated lqg control," *IEEE Trans. Control System Tech.*, 2019, (under review). [Online]. Available: https://rabraker.com/publication_pdf/braker_pao_tcst_2019.pdf

[50] G. M. Clayton, S. Tien, K. K. Leang, Q. Zou, and S. Devasia, "A review of feedforward control approaches in nanopositioning for high-speed spm," *Journal of Dynamic Systems, Measurement, and Control*, vol. 131, pp. 061 101–061 101–19, Oct. 2009.

[51] Z. Wang, A. C. Bovik, H. R. Sheikh, and E. P. Simoncelli, "Image quality assessment: from error visibility to structural similarity," *IEEE Trans. Image Processing*, vol. 13, no. 4, pp. 600–612, Apr. 2004.

[52] T. Ando, T. Uchihashi, and T. Fukuma, "High-speed atomic force microscopy for nano-visualization of dynamic biomolecular processes," *Progress in Surface Science*, vol. 83, no. 7, pp. 337 – 437, 2008. [Online]. Available: http://www.sciencedirect.com/science/article/pii/S0079681608000464

[53] J. Stirling and R. Woolley, "Scanning probe image wizard - matlab toolbox," https://sourceforge.net/projects/spiw/, accessed: 2019-4-27.